



# Mechanical Behavior Characterization of a Stainless Steel Dissimilar Metal Weld Interface : *In-situ* Micro-Tensile Testing on Carburized Martensite and Austenite

G. Ben Salem<sup>1,2,3</sup> · E. Héripéré<sup>2</sup> · P. Bompard<sup>2</sup> · S. Chapuliot<sup>1</sup> · A. Blouin<sup>1</sup> · C. Jacquemoud<sup>3</sup>

Received: 18 March 2019 / Accepted: 6 July 2020 / Published online: 27 July 2020  
© Society for Experimental Mechanics 2020

## Abstract

**Background** Stainless Steel Dissimilar Metal Welds (SS DMW) between low-alloy steel 18MND5 and austenitic 316L stainless steel are critical junctions in the currently operating reactors because of their heterogeneous microstructure and mechanical properties. The presence of a narrow hard layer of carburized martensite and austenite in the ferritic-austenitic interface creates an important hardness gradient which affects the crack behavior of the SS DMW.

**Objective** In order to evaluate the plastic properties of this hard layer, a micro tensile testing method was developed.

**Methods** Tensile specimens of 15 x 80 x 6  $\mu\text{m}$  were extracted from the martensitic and carburized austenitic layers by focused ion beam (FIB) micro-processing and tested using an *in-situ* tensile testing device. A platinum FIB deposition was used to measure local strain in the specimen during the test through digital image correlation (DIC). Isotropic elasto-plastic constitutive laws for the martensite and carburized austenite were obtained from the true strain-stress curves calculated from the micro-tensile tests.

**Results** It was found that the corresponding plastic properties were in a good agreement with nanoindentation measurements and with values obtained from macroscopic tensile tests on crossweld specimens machined perpendicularly to the ferritic-austenitic interface and characterized using laser beam local diameter measurements.

**Conclusions** *In-situ* tensile testing is a promising technique for plastic behavior characterization of small scale materials and local hard layers in dissimilar metal welds.

**Keywords** Dissimilar metal welds · Martensite · Carburized austenite · Plastic properties · Micro-tensile testing

## Introduction

Stainless Steel Dissimilar Metal Welds (SS DMW) between low-alloy steel 18MND5 (~A533) and austenitic 316L stainless steel are widely used within the French nuclear power plants, where they connect the main components to the primary circuit pipes (Fig. 1(a)). Because of their highly

heterogeneous microstructure, mechanical properties [1–3] and the existence of residual stresses [4], these components are critical for the integrity of the currently operating reactors [5–7].

The DMW under consideration is a 18MND5/316L weld with a 309L/308L buttering. The buttering is made on the ferritic component surface and then welded to a 316L stainless steel "safe-end" with a filling of the V groove by austenitic weld metal. The "safe-ends" are finally connected to the 316L stainless steel piping by onsite homogeneous welding (Fig. 1(b)).

The microstructure of these DMW was explored by F. Mas [1, 3] and characterized around the Ferritic-Austenitic interface in the as-welded state (after the welding process) and after a post-weld heat treatment at 610°C (PWHT) performed after welding to relax residual stresses in the weld metal (Fig. 2(a)). Between the ferritic heat

✉ G. Ben Salem  
ghassen.ben-salem@ecp.fr

<sup>1</sup> FRAMATOME, 1 Pl. Jean Millier, 92400, Courbevoie, France

<sup>2</sup> Laboratoire MSSMat, UMR CNRS 8579, CentraleSupélec, 3 Rue Joliot Curie, 91190, Gif-sur-Yvette, France

<sup>3</sup> DEN-Service d'études mécaniques et thermiques (SEMT), CEA, Université Paris-Saclay, F-91191, Gif-sur-Yvette, France



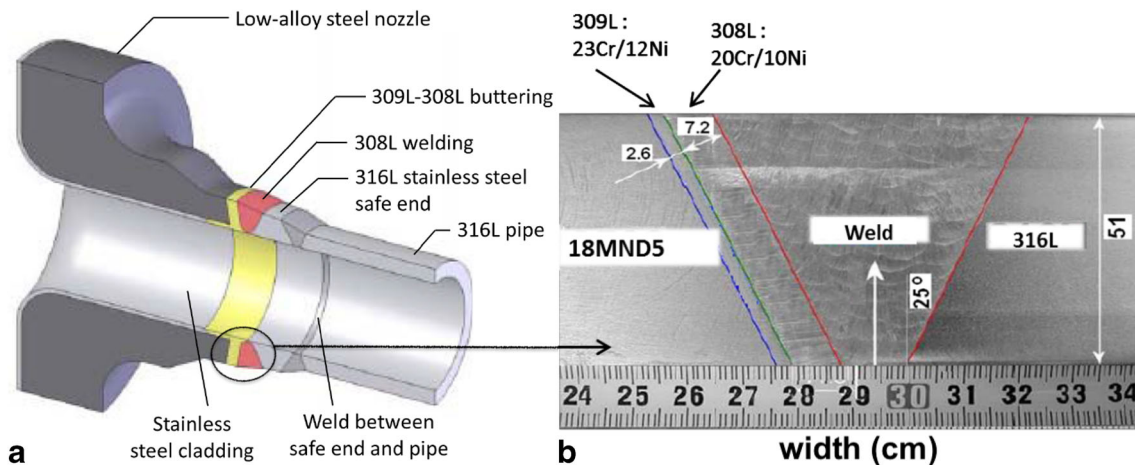


**Fig. 1** (a) Schematic of a connection between a low-alloy steel component and a stainless steel pipe; (b) Geometry and constituents of a dissimilar steel weld [1]

affected zone (HAZ) and the austenitic buttering, the author observed a thin transition layer, along the fusion line (FL) (interface between the ferritic HAZ and the fusion zone), which is composed of a thin martensitic layer and a fully austenitic zone of about  $100\ \mu\text{m}$  wide.

The martensitic layer formed at the interface results mainly from the carbon migration towards the austenitic weld metal combined with the local enrichment of Cr and Ni in the partially mixed zone due to the welding process and the stress relief heat-treatment [8–11]. Its phase identification can be performed by dilution calculations and the Schaeffer diagram [9, 12] or by means of Transmission Electron Microscopy observation [13–15]. High hardness was also measured in this martensitic layer [16, 17]. The fully austenitic zone shows a microstructure typical of a

primary austenite solidification grown on the ferritic base metal former heat treated austenitic grains, whereas the deposit material with a two-phase  $\delta$ - $\gamma$  dendritic microstructure is typical of a primary ferrite solidification [1].

After the welding process, the DMW undergoes a stress relief heat-treatment at  $610^\circ\text{C}$  for a duration between 3 and 16 hours (applied for SS DMW in the currently operating reactors). The main objective of this treatment is to relax the welding residual stresses in the bainitic HAZ and weld metal in order to avoid any brittle failure in these zones [18]. Mas [1, 3] shows that carbon diffusion from the ferritic low-alloy steel side (18MND5) to the austenitic high-alloy side (309L) is triggered at this temperature. The martensitic layer and the fully austenitic zone undergo a carbon enrichment together with nucleation and growth of carbides, generating

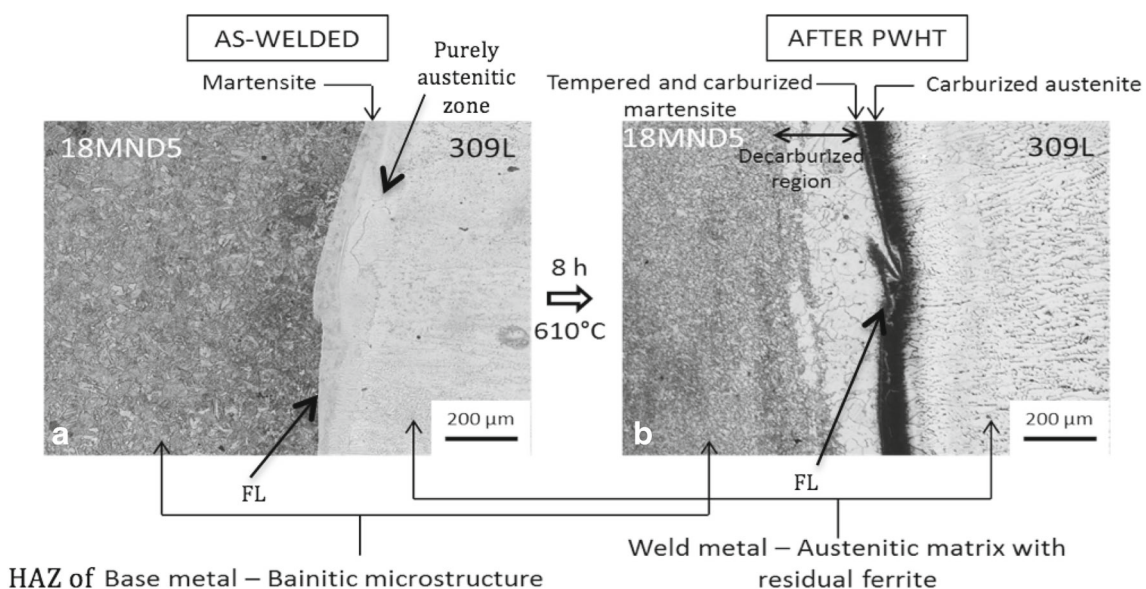


**Fig. 2** Optical micrograph of the dissimilar interface : (a) in the as-welded state (b) after PWHT [1]

a hard thin layer (between 50  $\mu\text{m}$  and 200  $\mu\text{m}$  width) of carburized martensite and austenite in the vicinity of a narrow decarburized ferritic band (Fig. 2(b)).

The resulting high mechanical properties gradients greatly affect the stress and strain distribution around the FL and the damage mechanism in a fracture test [1, 2, 6, 7], and coupled with the presence of a large population of defects (carbides at the grain boundaries), makes the 18MND5/309L interface a potential weak zone in the SS DMW. It is therefore necessary to characterize the mechanical behavior of the hard layer and to precisely measure the plastic properties variation (yield stress and hardening exponent) around the FL in order to correctly model the overall transverse behavior of the DMW.

Plastic behavior characterization of the hard layer where tensile specimens can not be extracted is a real challenge in SS DMW. In addition to their limited width, the important local hardness in comparison to the surrounding soft layers (ferritic decarburized HAZ and austenitic buttering) prevents any plastic deformation in a macroscopic tensile specimen machined perpendicularly to the FL [1]. Nanoindentation, which is a local method to probe mechanical properties at a submicron scale, seems to be suitable for this case but presents many limitations: plastic properties are identified by reverse algorithm based on functions originating from finite element (FE) simulations which are performed with some assumptions (perfectly shaped indents, low hardening capacity...). Furthermore, this method gives highly dispersed results for materials with heterogeneities whose size is comparable to the indent size or with coarse microstructure [1].

On the other hand, micro-tensile testing has proven to be a valuable technique to directly characterize materials at small dimensions and measure the strain-stress curve up to failure. In the past, a few tensile tests have been performed especially on single crystal specimens, such as those conducted on single-crystal copper specimens by Kiener et al. [19] to explore the size-dependance of crystal plasticity, or on single-crystal Fe samples by Bhattacharyya et al. [20] to observe slip phenomena. The effect of irradiation on materials was also studied by *in-situ* micro tensile testing on irradiated and implanted single crystal nickel films by Reichardt et al. [21] or on irradiated stainless steel by Vo et al. [22]. Katsuhiko et al. [23] also performed *in-situ* tensile tests on bi-crystal Fe-Mn-P alloy specimens to evaluate the grain boundary strength after P segregation.

However, the use of this technique on thin regions has been quite challenging and several experimental hurdles had to be overcome to do proper tensile testing of materials in the meso-scale dimension regime (i.e. a range of a few  $\mu\text{m}$  to tens of  $\mu\text{m}$ ). The manufacturing of sensitive equipment for the test (grips), the fabrication of the specimen or

the choice of measurement methods for stress and strain calculation are among the technical difficulties which have to be taken into account to properly measure mechanical properties.

The present study aims to present a new characterization method with *in-situ* tensile testing to measure the plastic properties of the martensitic and carburized austenitic layers. The samples were extracted from the different layers with FIB micro-processing and tested using a home-made *in-situ* micro-tensile testing machine. The measured values for the yield stress and hardening exponent are compared to the elasto-plastic constitutive laws identified by nanoindentation in the literature [1, 2] and by macroscopic tensile testing on tensile specimens machined perpendicularly to the FL and characterized using laser beam diameter measurement along the specimen.

## Experimental

### Experimental Mock-up

The DMW mock-up used in this study is a 18MND5 (SA 533)/316L weld with a 309L/308L buttering (Fig. 3), typical of DMW between steam generators and the primary circuit piping of the currently operating reactors. The buttering is made on a ferritic plate and is composed of several layers (i.e., the first layer is made of 309L weld metal, the rest are made of 308L weld metal), then, the buttering is welded to a 316L stainless steel plate with a filling of the V groove by austenitic weld metal.

The 308L/309L buttering, which has a total width of approximately 15 mm, was deposited using a TIG welding with a voltage of 12.5 V and an intensity of 350 A, the deposited material being the material used as the electrode. As for the weld between the buttering and the 316L austenitic steel plate, the width is close to 15 mm and the weld was performed using a TIG welding with a voltage of 13 V, an intensity of 219 A, and a 308L austenitic stainless

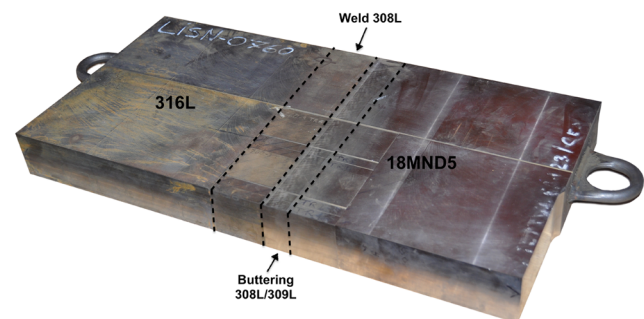


Fig. 3 Stainless steel dissimilar metal mock-up for tensile testing

steel as filler material. Finally, a post-weld heat treatment at 600°C for 3 hours was applied to the DMW mock-up in order to relax the welding residual stress. The chemical compositions of base metals and filler materials is given in Table 1.

The microstructure around the 18MND5/309L interface was explored using SEM imaging, EDS measurements and EBSD analysis. The important hardness gradient in the vicinity of the interface, reported by F. Mas [1] in the heat treated state, was also characterized with Vickers micro-indentation profiles perpendicular to the interface.

### Tensile Testing of Crossweld Specimens

In order to characterize the welded junction, smooth specimens were machined in the SS DMW mock up through the buttering weld (crossweld) (Fig. 4). A new measurement system, developed in the LISN laboratory of the CEA (French atomic commission) by Ancelet [24], was used to test the crossweld specimens. The use of two laser micrometers equipped on a tensile machine allows measuring the local diameter variation along the specimen during the tensile test.

The axial stress and strain are then calculated locally along the tensile axis using the following formulas for an axisymmetric tensile specimen :

$$\epsilon = \ln \left( \frac{S_0}{S} \right) = -2 \ln \left( \frac{a}{a_0} \right) \quad (1)$$

$$\sigma_{true} = \frac{F}{S} \quad (2)$$

where  $\epsilon$  and  $\sigma_{true}$  are the local strain and stress,  $a$  is the specimen local radius,  $a_0$  the specimen initial radius,  $F$  is the load and  $S$  the local section.

Moreover, a Bridgman correction of the true stress is performed for the specimen position where necking occurs using the following formula :

$$\sigma_{true} = \frac{F}{S} \cdot B \left( \frac{a}{R} \right) \quad (3)$$

where  $B$  is a Bridgman function to take into account the stress multiaxiality due to the local curvature  $R$  during the instability phase (necking) [24].

**Table 1** Chemical compositions of base metals and filler materials

	C	Si	Mn	Ni	Cr	Mo	Fe
18MND5 (wt %)	0.182	0.236	1.53	0.639	0.153	0.506	bal.
316L (wt %)	0.025	0.370	1.98	10.15	17.08	2.14	bal.
309L (wt %)	0.02	0.5	1.7	13.0	24.0		bal.
308L (wt %)	0.02	0.5	1.7	10.0	20.0		bal.

For the crossweld specimen, this measurement system was used to calculate a true strain-stress curve for each material and a constitutive behavior law was obtained for each macroscopic layer (ferritic base metal, ferritic HAZ, austenitic buttering, austenitic weld) assuming that the materials have an isotropic elasto-plastic behavior. In this context, the yield criterion is adopted as the criterion of von Mises.

It must be noted that only the axial stress (in the tensile direction) is considered in the previous stress formula. So in order to extract the plastic properties of the material from the experimental strain-stress curve, we have to verify that shear stress remains negligible, which is the case for the macroscopic layers in the crossweld specimen, but not for thin hard layers subjected to transverse compression.

The austenitic buttering 308L/309L being softer than the ferritic steel, crossweld specimens with a homogeneous diameter (8 mm) (Fig. 4(b1)) are used to characterize the austenitic side of the weld. Specimens with variable diameters (smaller diameter of 7.2 mm in the ferritic side vs 8 mm in the austenitic side) (Fig. 4(b2)) allow the deformation of the ferritic base metal and HAZ and are therefore used to characterize the ferritic side of the weld. The diameter variation of these specimens was optimised with numerical simulation of the tensile tests using the constitutive behavior laws identified for the DMW different layers by F. Mas in [1]. All tensile tests on crossweld specimens were performed at room temperature.

### In-situ Tensile Tests

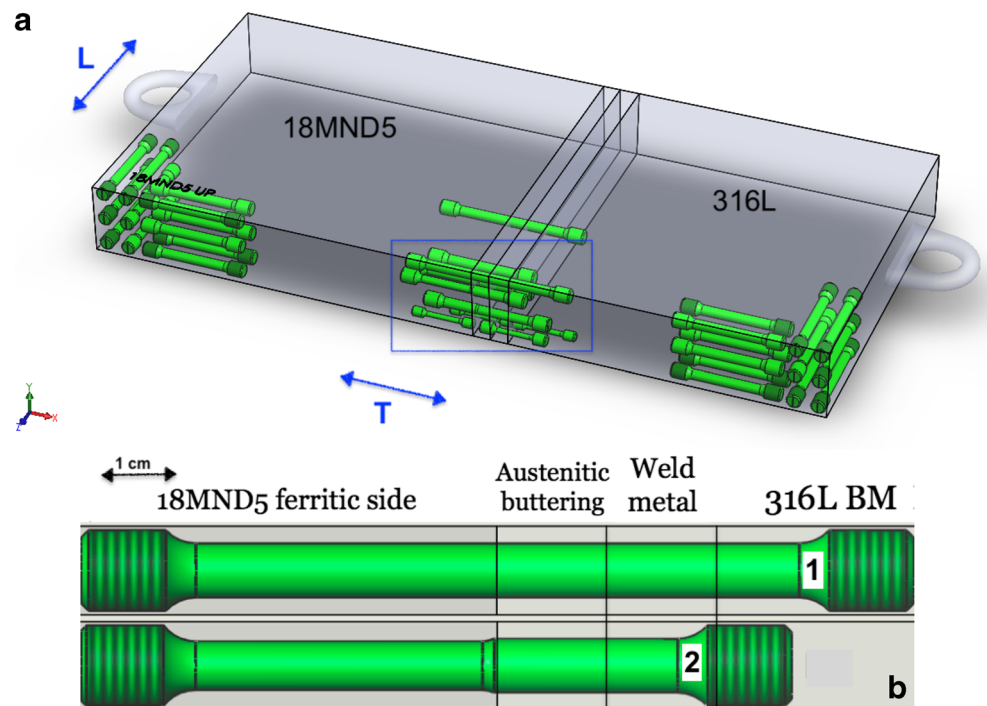
The objectif of *in-situ* tensile tests is to characterize the mechanical behavior of layers where homogenous macroscopic tensile specimens can not be extracted because of their limited width, such as the martensitic and carburized austenitic layers. Furthermore, in the case of these thin layers, the important local hardness prevents any plastic deformation during a tensile test on a crossweld macroscopic specimen.

In this context, the testing of specimens from the martensitic band or the carburized austenite requires several precautions. Because of the limited width of these layers, the specimens had to be entirely machined and tested separately from the macroscopic weld sample, which required the machining of two grips on both sides of the specimen. The following requirements had to be taken into account in order to do a proper *in-situ* tensile testing on these materials:

- Small specimens with a tensile geometry (dogbone for example) must be fabricated separately from the original macroscopic sample;



**Fig. 4** (a) Machining of tensile specimens in the SS DMW mock-up (b) zoom on crossweld specimens: 1) crossweld specimen with homogeneous diameter and 2) crossweld specimen with variable diameter



- Special attention must be given to the specimen manipulation to avoid losing it during the test preparation;
- Two grips must be machined separately from the specimen;
- The specimen has to be fixed in the grips during the tensile test;
- Loads and displacements have to be measured during the test.

To answer these needs, a micro-testing machine was developed in the MSSMat Laboratory with the collaboration of Framatome. The specimens were fabricated using a FEI Helios Nanolab 660 FIB/SEM equipped with an easylift micromanipulator and a gas induced system for Platinum deposition. They were then tested on the micro-tensile device.

### *In-situ* tensile machine

The testing machine used for the *in-situ* tensile tests is presented on Fig. 5.

The machine frame was 3D printed with plastic materials and specific parts were machined to fix the different components for the specimen and grips machining. The frame was also covered with an electrically conductive spray paint to avoid drift issues during electronic and ionic imaging or EDS and EBSD measurements.

A load cell with a capacity of 50 g (0,5 N) was used to measure loading during the test. The load sensor was calibrated using equipment traceable to NIST (National

Institute of Standards and Technology) and a calibration certificate was provided. A Molybdenum thin foil (a lift-out grid was used) (Fig. 5 & 6) was fixed on the load cell side of the tensile device and was used to machine one of the specimen grips (grip on the right side of Figs. 6 & 9). The fixing component containing the lift-out grid was attached to the extremity of the strain gauge load cell so that the load is transmitted from the specimen to the load cell via the lift-out grid during the tensile test. The other specimen grip (grip on the left side of Figs. 6(b) & 9) was machined in a tungsten needle mounted on a rotating motor (Fig. 5), which is also necessary for the specimen fabrication.

Finally, the displacement in each direction was obtained with piezoelectric displacement plates (Fig. 5) characterized by a displacement resolution of 1 nm and a speed resolution of 1  $\mu\text{m/s}$ . The loading direction (X direction) was also controlled with an encoder to precisely measure the specimen displacement during the test. More details on the *in-situ* tensile machine components and the sample preparation are given in [25].

### Sample preparation

In order to distinguish the martensitic layer and fully austenitic zone in the interface, a weld sample was prepared by classical polishing techniques, the last step consisting of prolonged polishing in a colloidal silica suspension which reveals the martensitic laths and the ferritic grains in the ferritic HAZ (Fig. 7). The polishing also clearly reveals the ferritic dendrites in the austenitic side making it possible to

**Fig. 5** (a) *In-situ* micro-tensile testing machine (b) 3D representation of the *in-situ* micro-tensile testing machine

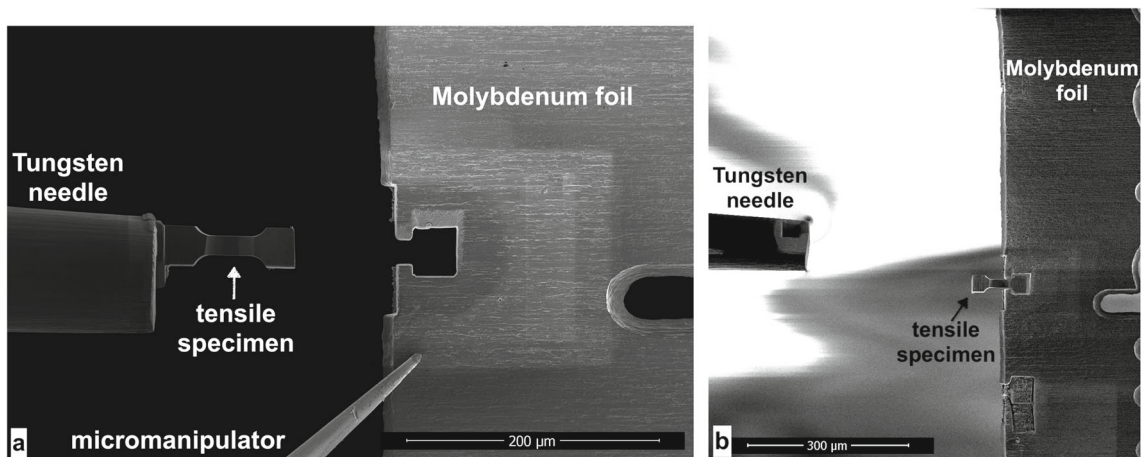
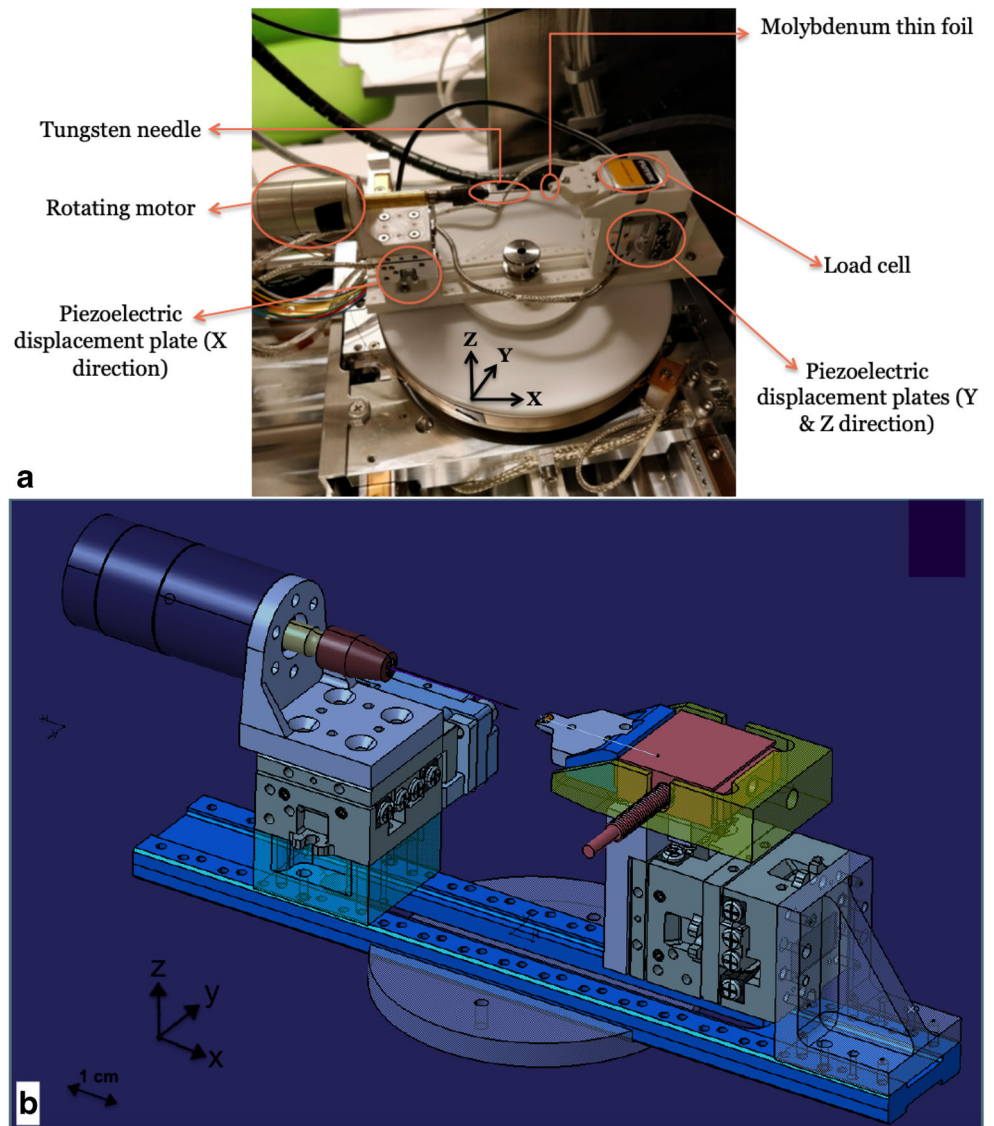


**Fig. 6** SEM image of the tensile device after (a) specimen preparation and first grip machining in the molybdenum foil (b) second grip machining in the tungsten needle

distinguish the fully austenitic zone from the two-phase  $\delta$ - $\gamma$  microstructure of the buttering.

The first step for the specimen machining was the extraction of a block ( $30 \times 100 \times 15 \mu\text{m}$ ) from the sample with FIB milling. The extracted block was welded to a micromanipulator needle (Fig. 6(a)) and then transported and welded to the rotating needle tip with FIB induced deposition of Pt. The tensile specimen was finally machined by rotating the needle mounted on the rotating motor (Fig. 6(a)). In addition to the specimen machining, it was also possible with the help of the needle rotation to perform electronic and ionic images and Electron Backscatter Diffraction (EBSD) measurements on the specimen surfaces to confirm the position of the different layers within the specimen and give data for crystal plasticity.

The second step consisted of the first grip machining in the Molybdenum thin foil (Fig. 6(a)). Then using the three piezoelectric displacement plates, the tensile specimen was inserted in the machined grip (Fig. 6(b)). In order to fix the specimen, the chamfers were welded to the grip with a platinum layer. In this configuration, the welds remained under compression during the tensile test to have a higher resistance. Once the specimen was fixed in the molybdenum grip, the second grip was machined in the rotating needle tip after ensuring that the tip diameter was suitable with the grip dimensions (Fig. 6(b)).

The final step was the insertion of the second machined grip in the welded specimen head by using the three displacement plates (Fig. 9(a)). It must be noted that the head was not welded to the second grip in order to ensure some flexibility for the specimen. A preload was also applied before each tensile test to align the specimen gauge length with the tensile direction and to minimize the off-axis loading during the test.

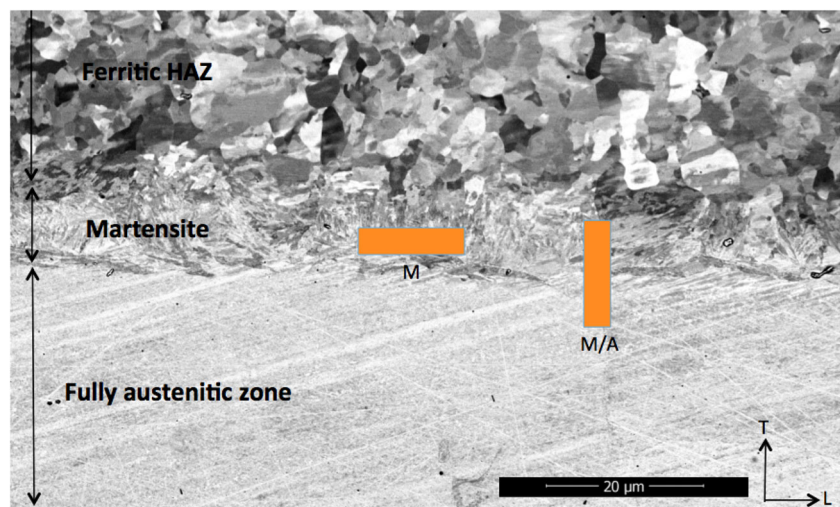
In this study, two dogbone tensile test specimens were machined in a weld sample from the SS DMW mock-up. The first machined specimen was extracted from the martensitic band in the longitudinal direction L (specimen M in Fig. 7) and the gauge section dimensions (width =  $15 \mu\text{m}$ , length =  $35 \mu\text{m}$  and thickness =  $6 \mu\text{m}$ ) were chosen in order to obtain a homogeneous martensitic composition and to have an estimated failure load under the upper limit of 0.5N of the load cell. The martensitic laths shown in Fig. 8(a) confirm the homogeneity of the martensitic specimen.

The second machined specimen (specimen M/A in Fig. 7) was extracted in the martensite/austenite interface in the transverse direction T with the same dimensions to be able to use the same machined grips. Given the important size of the austenitic grains in the fully austenitic zone (up to  $100 \mu\text{m}$ ), it was not possible to have more than a single austenitic crystal from the carburized austenite in the specimen which we can clearly distinguish from the martensitic laths in the martensitic side (Fig. 8(b)). The martensite/austenite interface also seems to be very irregular, being well centered on the upper side of the specimen and shifted to the austenitic side in the lower side.

It must be noted that an observation with secondary electrons given by ion scanning revealed the crystals boundaries of both the martensitic and austenitic parts of the specimens thanks to the channelling effect [26], as shown in Fig. 8. However, a long exposure to ion scanning had to be avoided in the austenitic steel since  $Ga^+$  ions can induce a  $\gamma \rightarrow \alpha$  transformation as it has been reported in [27–29].

The homogeneity of the martensitic specimen was confirmed by EDS after testing by comparing the measured local chemical composition in the specimen to EDS measurements in the martensitic band from a macroscopic

**Fig. 7** SEM image of 18MND5/309L interface after colloidal silica polishing (5 kV, BSE) and tensile specimens sampling (M : martensitic specimen, M/A : Martensite/Austenite specimen)



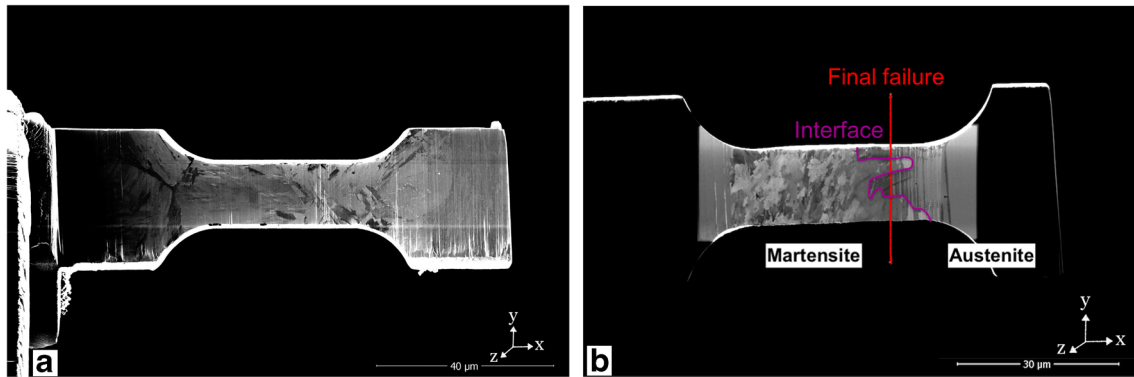


**Fig. 8** (a) Martensitic specimen before testing (b) Martensite/Austenite specimen before testing. The red line indicates the final failure location in the specimen and the purple line indicates the martensite/austenite interface

weld sample. In addition to EDS probing, EBSD was performed on the martensite/austenite specimen to confirm the interface localization and to obtain the austenitic crystal orientation. The austenitic grain had a  $\sim[102]$  orientation along the normal direction (perpendicular to the specimen surface) and a  $\sim[001]$  orientation along the tensile axis. The corresponding maximum Schmid factor along the tensile axis of the specimen was equal to 0.49, indicating that the austenitic crystal orientation was favorable to slip systems activation and plastic deformation during the tensile test. It should also be specified that the austenitic crystal orientation is in agreement with the solidification direction in the fully austenitic zone (along the temperature gradient so perpendicular to the ferritic-austenitic interface), which explains the important grain size.

### Strain and stress measurements

In order to measure the local and global plastic deformation during the tensile test, several arrays of platinum spots separated by  $0.5 \mu\text{m}$  were induced by FIB deposition on

the surface of the specimen (Fig. 9(b)). High definition SEM images ( $3072 \times 2048$  pixels) with a sufficiently low noise level were acquired at small strain intervals during the tests with a secondary electron detector using a dwell time of about  $10 \mu\text{s}$ , leading to a total recording time of about 60 s per image, during which the loading was stopped. CMV, a DIC software [30], was then used to calculate the displacement field in the specimen surface for each SEM image. The used mesh for the local displacement calculation was defined in the reference image such as the correlation windows were centred on each spot of the FIB induced marking. The local plastic strain field and the average strain in the specimen were derived from the displacement field with CMV according to the method developed in [31] and based on the computation of the in-plane components of the deformation gradient  $F$  relative to various gage lengths, from which various strain components can be derived.

For each test, a true strain-stress curve was calculated from the load cell data and the SEM images measurements. To calculate the true stress, the specimen section was measured for each image in the region where the final

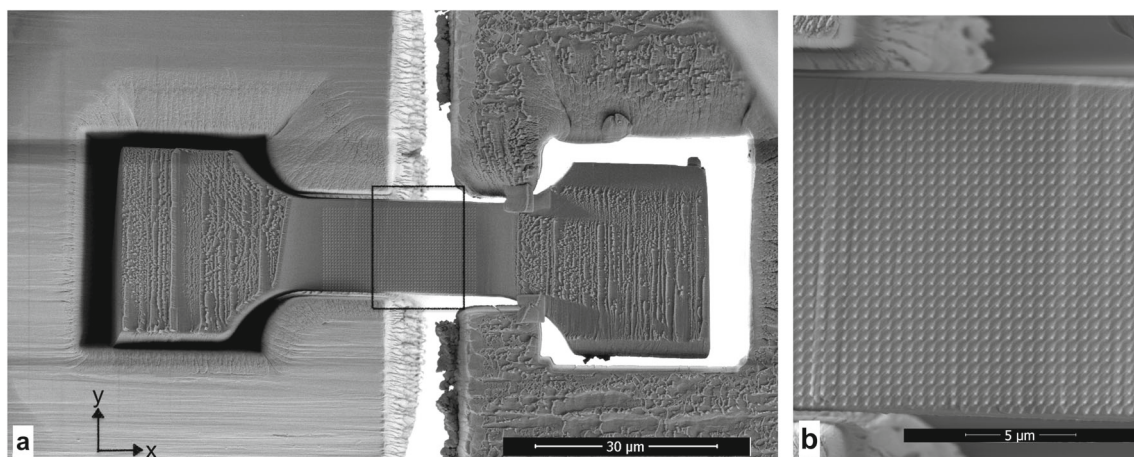


**Fig. 9** (a) SEM image of the tensile specimen after insertion in the grips and marking by platinum FIB deposition (b) zoom in on the FIB marking



failure occurred by assuming that the relative variation of the specimen thickness is equal to the measured width variation (isotropic plastic behavior).

For the true strain calculation, DIC measurements were only possible for a limited range of strain because of the rather high strain rate of both specimens compared to the SEM image acquisition time. For the martensitic specimen, no images could be taken in the plastic phase while for the martensite/austenite specimen, the last image taken before failure led to a calculated true strain of 10.5% (Fig. 17(a)). Moreover, the thin FIB deposited Pt layer showed some cracks in the plastic phase for both specimens (Figs. 15 & 16), making post failure DIC measurements impossible in some parts of the specimen surface.

Three additional methods were therefore tested and compared to DIC measurements. The specimen gauge section where final failure occurs, the gauge length and the distance between the two grips were measured for each SEM image taken during the test. Moreover, in order to characterize the specimens plastic behavior after the last SEM image taken during the test, some additional images were extracted from the test videos for greater strain values. The true strain was then calculated based on the variation of these three parameters using the following formula :

$$\epsilon_{section} = \ln\left(\frac{S_0}{S}\right) \quad (4)$$

$$\epsilon_{length} = \ln\left(\frac{l}{l_0}\right) \quad (5)$$

$$\epsilon_{grips} = \ln\left(\frac{l_0 + \Delta d_g}{l_0}\right) \quad (6)$$

where  $\epsilon_{section}$ ,  $\epsilon_{length}$  and  $\epsilon_{grips}$  are respectively the true strain calculated from the gauge section  $S$ , gauge length  $l$  and the variation of the distance between the grips  $\Delta d_g$ .

## Results

### Micrographic Study of the DMW

Based on SEM imaging (Fig. 7), EBSD analysis (Fig. 10(a)) and EDS profiles (Fig. 10(b)) performed on a crossweld sample after polishing and chemical etching, the different microstructures around the Ferritic-Austenitic interface were characterized:

- On the ferritic base metal side (18MND5), a Heat Affected Zone characterized by its bainitic microstructure is formed.
- A transition layer, along the fusion line, which is composed of a thin martensitic layer and a fully austenitic zone of about 50  $\mu\text{m}$  wide.
- On the weld metal side (309L), the austenitic buttering is characterized by its two-phase  $\delta$ - $\gamma$  microstructure and the presence of dendrites.

The martensitic layer has a variable width between 10 and 100  $\mu\text{m}$  approximatively, which is due to the convection flow and local chemical composition in the molten pool during the welding of the austenitic buttering, generating in some areas martensitic islands within the austenitic layer as seen in Fig. 10(a). Energy Dispersive X-ray Spectrometry (EDS) measurements across the ferritic-austenitic interface (Fig. 10(b)) reveal the presence of an intermediate zone, whose chemical composition corresponds to a mixture between mainly the ferritic steel and the austenitic buttering. This intermediate zone corresponds to the martensitic band since it is situated between the ferritic HAZ, whose chemical composition is the same as the ferritic base metal, and the fully austenitic zone, which is characterized by the absence of dendrites. The EBSD analysis in Fig. 10(a) shows the grain size around the ferritic-austenitic

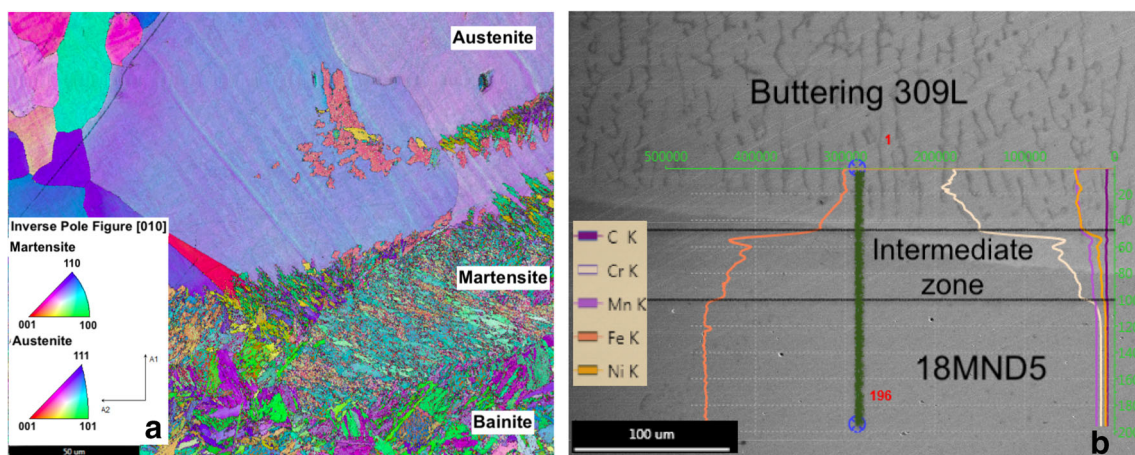


Fig. 10 (a) EBSD profile across the 18MND5/309L interface (b) EDS profile on a line across the 18MND5/309L interface

interface. In the martensitic band, the laths have a limited size ( $<10\ \mu\text{m}$ ) and are much smaller compared to the carburized austenitic grains. The austenitic side has a coarse microstructure with important grain size, which appears to be very heterogenous near the martensitic band varying between around 20 and  $100\ \mu\text{m}$ .

The evolution of hardness across the 18MND5/309L interface was also characterized in Fig. 11 and shows, as reported in [1], an important hardness gradient caused by the carbon diffusion from the ferritic side to the austenitic buttering during the PWHT. The peak hardness is generally obtained at the interface between the martensitic and the austenitic layers and decreases rapidly in the fully austenitic zone.

However, the presence of a decarburized ferritic HAZ in the ferritic side with a lower hardness value is not clearly visible in the hardness profiles, even though a slightly lower value is obtained between the martensitic layer and the ferritic HAZ (Fig. 11). This could be due to the layer's limited width compared to the indenter size.

In the following sections, the objectif is to characterize the tensile properties of the observed hard layer composed of the martensitic layer and the carburized austenitic zone.

### Tensile Testing of a Smooth Crossweld Specimen

Macroscopic crossweld specimens machined in the DMW mock-up were tested at room temperature and behavior constitutive laws for each layer in the tensile specimens were determined from a laser measurement of the local diameter variations during loading. Figure 12 shows an example of behavior constitutive laws identification with the crossweld specimen with variable diameter. The ferritic base metal, ferritic HAZ, austenitic buttering and weld metal were characterized using the profilometry measurement during the tensile test. The local diameter variation in the hard layer (martensitic band and carburized austenite) is negligible compared to the much softer layers near the interface (decarburized HAZ and austenitic

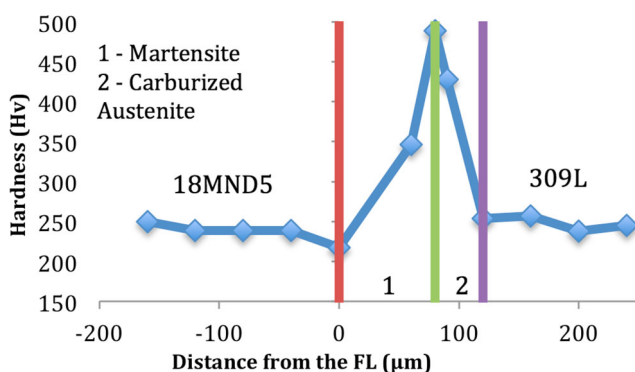


Fig. 11 Micro-hardness profile around the FL

buttering). This strain gradient creates important shear stress in the hard layer and a direct identification of a constitutive behavior law is therefore not possible in the same way than for the macroscopic layers.

In order to identify the plastic properties and a constitutive behavior law for the hard layer, a reverse method using numerical simulation was applied.

The tensile test of the specimen with variable diameter (Fig. 12(a)) was modeled using a finite element analysis with Cast3m software [32]. The mesh used for the modeling and the associated layers and boundary conditions are presented in Fig. 13(a). The modeling was performed with 2D axisymmetric calculation using quadratic elements QUA8 and assuming large strains and large displacements. The boundary conditions were as following:

- All the displacements are locked for line CD;
- The line EC is the axisymmetric axis;
- The loading displacement along the tensile axis is imposed on line EF.

The material behavior for each of the four macroscopic layers was given by the constitutive laws in Fig. 13(a) and their width was determined based on the profilometries measurements during the tensile test (Fig. 12(a)). For the hard layer, a perfectly plastic behavior law with no hardening was assumed for both the martensitic and carburized austenitic layers. The position of the martensitic/austenitic interface was measured on the specimen after chemical etching to reveal the FL and the width of the hard layer ( $120\ \mu\text{m}$ ) was measured with a hardness profile across the interface (Fig. 11).

The numerical model was validated by comparing the experimental and numerical engineering strain-stress curves until failure as well as the diameter profilometries calculated numerically and measured with the two laser micrometers at two different moments in the tensile test: when the load reached its maximum value, and at failure (Fig. 13(b)). The good agreement between tests and computation results validates the constitutive behavior laws used in the numerical model for the different layers in the SS DMW.

Using the validated model, several simulations were performed with different yield stress values for the hard layer. For each simulation, local strain-stress curves were calculated using equations (1) & (2) at different positions in the hard layer: on the FL and at  $75\ \mu\text{m}$  from the FL in the martensitic layer. These curves were then compared to the corresponding experimental curves.

Figure 14 shows that a good agreement was obtained for a yield stress of 1800 MPa for the two positions at the FL and at  $75\ \mu\text{m}$  in the hard layer. The numerical and experimental curves are also similar after the yielding point which validates the perfect plasticity assumption of

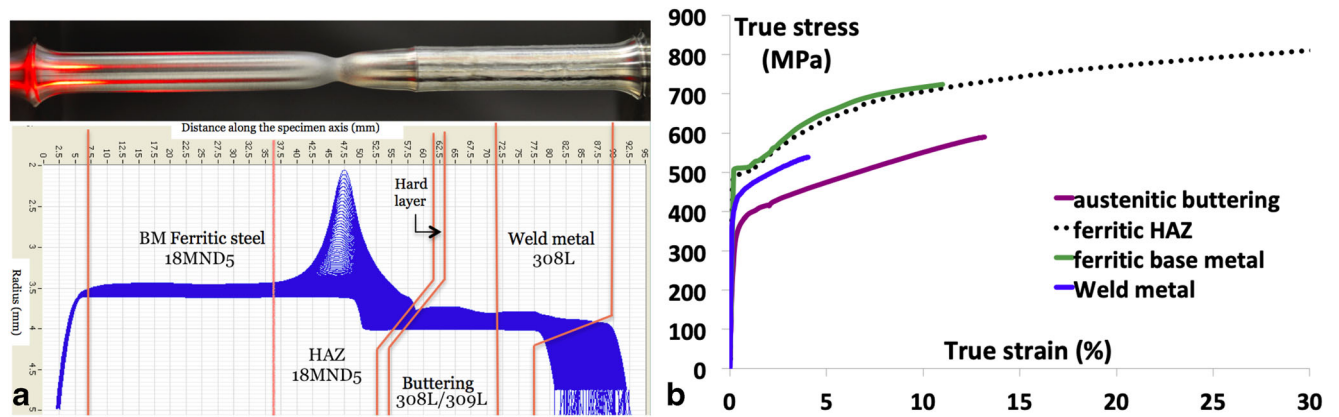


Fig. 12 (a) Profilometries measurement during the tensile test on a crossweld specimen with variable diameter (b) Constitutive isotropic elasto-plastic laws calculated for the macroscopic layer of the SS DMW

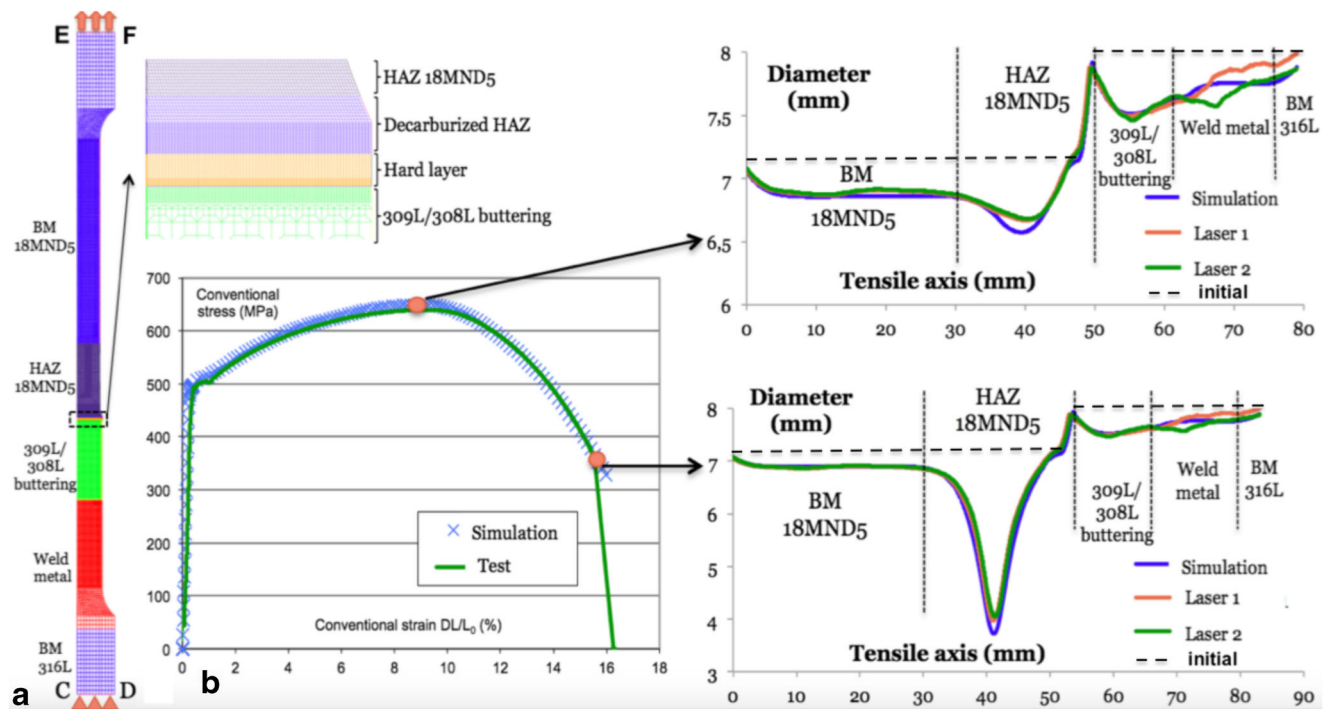
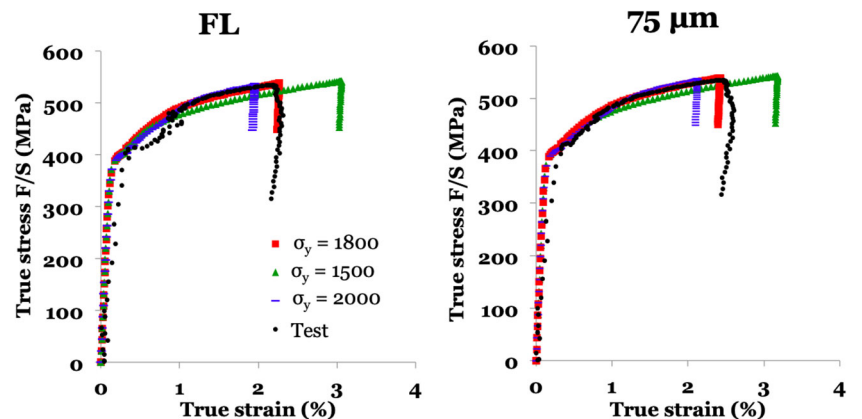


Fig. 13 Numerical simulation of the crossweld specimen with variable diameter : (a) Numerical model mesh and boundary conditions (b) Comparison between experimental and numerical engineering stress-strain curves and diameter profiles

Fig. 14 Comparison between experimental and numerical true stress-strain curves at different positions in the hard layer for different hard layer yield stresses a) on the FL and b) at 75 μm from the FL



the hard layer made for the numerical simulations. It must be specified that the calculated value of 1800 MPa is an estimated yield stress for the hard layer, without making the distinction between martensitic and carburized austenitic layers.

### Mechanical Characterization of the Hard Layer with *In-situ* Tensile Testing

Two micro-specimens were extracted from the martensitic layer parallel to the 18MND5/309L interface and in both martensite and austenite perpendicularly to the interface (Fig. 7). The two specimens were tested to failure and videos of the tests were recorded. The displacement was held constant during the image acquisition and each pause was accompanied by a stress relaxation ranging from 5 to 10 MPa.

Figure 15(a) shows the martensitic specimen after failure. Significant necking was exhibited in both specimens and shows that both materials have a ductile behavior reaching local plastic deformations (calculated for a square of  $0.5 \times 0.5 \mu\text{m}$  around each spot) around 30% for the martensitic specimen and 80% for the martensite/austenite specimen. For the bimaterial specimen, plastic deformation was concentrated in the austenitic side and the martensitic side remained elastic during the test (Fig. 16) and exhibited a higher resistance than the carburized austenite.

Moreover, the martensitic specimen reached failure immediately after the start of plastic deformation confirming the material's very small hardening capacity, while the austenitic side of the bimaterial specimen underwent significant work hardening after yield. The ductile behavior of the martensitic layer and carburized austenite was confirmed by the observation of the fracture surfaces of both specimens. Small dimples were observed in the martensitic specimen (Fig. 15(b)) which are due to the numerous carbides in the material, while no clear dimples were observed

in the carburized austenite which is due to the very large section necking.

For the martensite/austenite specimen, the calculated true strain-stress curves using the different strain calculation methods are presented in Fig. 17(a). Only the austenitic side of the specimen was considered for the strain calculation, so the martensitic phase was not considered in the gauge length measurements or for strain calculation with the DIC software. DIC measurements are in a good agreement with strain calculation based on the section and gauge length variation, while the calculation based on the variation of the distance between the grips predicted higher strain values. This is due to the specimen slip in the grips in addition to the failure of the welds between the specimen and the molybdenum grip during the test. The strain calculation based on the specimen gauge section variation was finally selected to identify the constitutive laws for both the martensitic and carburized austenite layers.

A Bridgman correction of the stress as in equation (3) was also applied for this test to take into account a possible multi-axiality effect, but no significant difference was found.

Figure 17(b) shows the true strain-stress curves for both tests. The martensitic specimen exhibited a yielding point at 1680 MPa ( $\pm 100$  MPa) as there was a clear deviation from linear elasticity at a strain of  $\sim 1\%$ . The maximum stress of 1900 MPa is reached at failure immediately after yield, so no hardening was measured for the martensite.

The second test characterized the carburized austenite since only the austenitic side of the specimen underwent plastic deformation, the martensitic side remaining elastic. The calculated true stress at specimen failure in the martensitic side of the specimen was only  $\sim 900$  MPa which is smaller than the yield strength of 1680 MPa calculated for martensite in the first test. It must be pointed that for the martensite/austenite specimen, final failure occurs in a plane mixing carburized austenite and martensite (Fig. 8(b)), which was tracked by the FIB deposition marking. For the

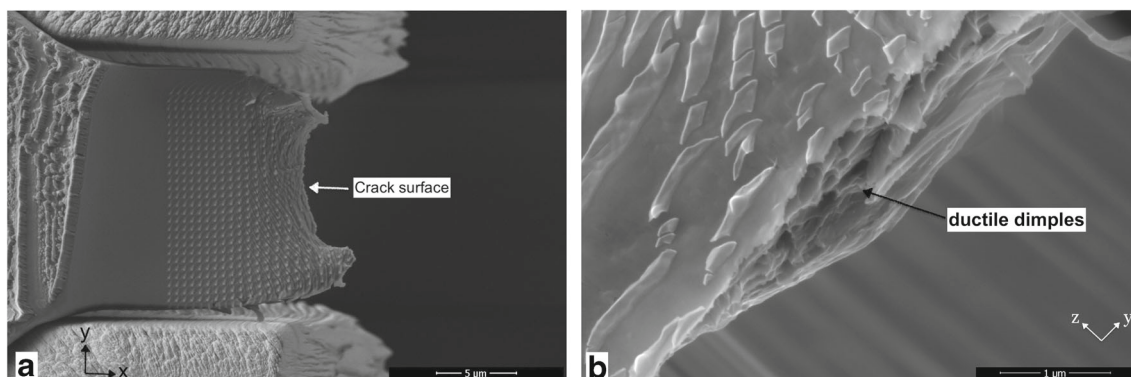
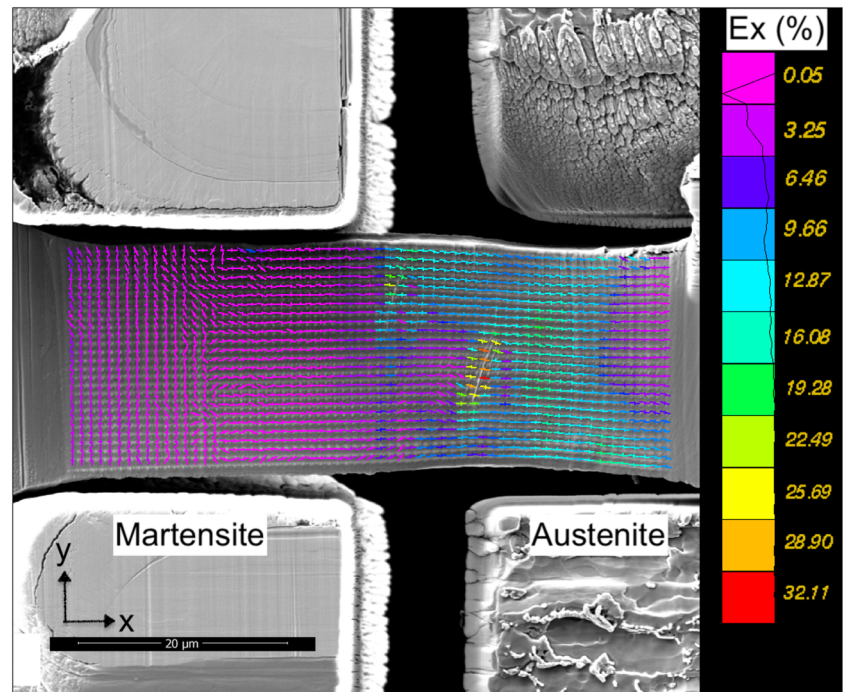


**Fig. 15** (a) Martensitic specimen after failure (b) crack surface of the martensitic specimen with ductile dimples

**Fig. 16** Strain repartition (along the x axis) in the Martensite/Austenite specimen in the necking phase ( $\sigma = 915$  MPa (in the necking zone) et  $\epsilon = 10,5\%$ )



carburized austenite, a clear deviation from linear elasticity is measured at a strain of  $\sim 1.5\%$  and a stress of 620 MPa. The yielding point was confirmed by DIC measurement as a clear disparity between strain values in martensite and carburized austenite initiated at that point. The austenitic side then underwent an important work hardening ( $n = 0.25$ ) and reached a stress of  $\sim 2000$  MPa at failure. The final reached stress was therefore greater than the yield strength of the martensitic layer which is in agreement with the specimen failure in both martensite and carburized austenite.

## Discussion and Comparison of the Different Characterization Methods

The tensile properties of the hard layer identified from tensile tests on crossweld specimens and from *in-situ* tensile tests on FIB machined samples were compared to nanoindentation results from F. Mas study in [1] for validation.

### Nanoindentation [1]

Mas [1, 2] probed the plastic properties of thin layers (decarburized ferritic HAZ, Martensite, Carburized austenite), where tensile specimens could not be extracted, with nanoindentation. It must be noted that the SS DMW mock-up used in [1, 2] was realised with the same materials

(18MND5, 308L and 309L) used in the mock-up of this study, but with a Submerged Arc Welding (SAW) technique and a longer PWHT (8 hours). However, the difference in these parameters is not expected to generate a significant difference in the mechanical properties of the hard layer of both SS DMW mock-ups.

Two different indenters (Berkovich and cube corner) were used and the local plastic properties were identified by reverse algorithm based on Bucaille's method [33] with correction for friction. The method required each Berkovich indent to be associated with another cube corner indent to determine one set of plastic properties (yield strength  $\sigma_y$ , hardening exponent  $n$ ). The results obtained are summarized in Table 2.

The results show a high scatter in the Martensite and carburized austenite which is due to the heterogeneous microstructure and the presence of a large population of carbides. Moreover, an important drop of hardness occurs in the carburized austenite when moving towards the stainless steel away from the martensite/austenite interface. This layer had therefore to be divided into two subregions characterized by a strong gradient in mechanical properties: a mean  $\sigma_y$  value of 2300 MPa and  $n = 0$  at 15  $\mu\text{m}$  from the martensitic band and a much softer region at 40  $\mu\text{m}$  with a mean  $\sigma_y = 1000$  MPa and  $n = 0.12$ . The martensitic band is characterized by a mean yield strength of 1650 MPa and doesn't show much hardening ( $n = 0$ ).

Although these values give a good indication of the local plastic behavior in the hard layer, some uncertainty

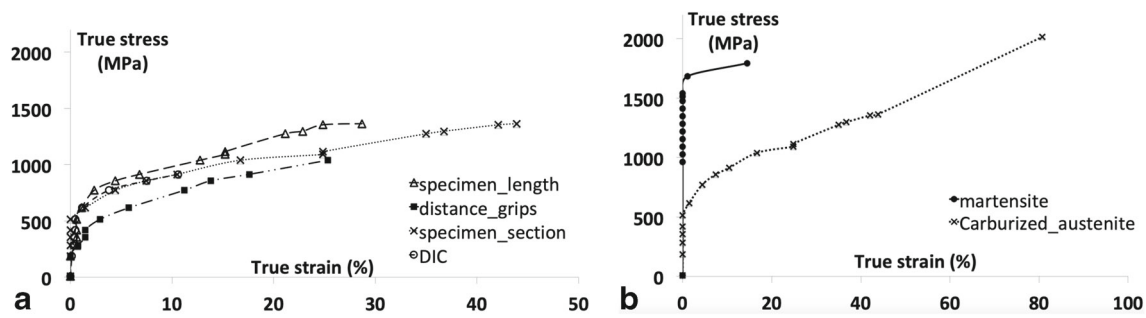


**Fig. 17** (a) Comparison between the different methods of true strain calculation for the carburized austenite (b) True strain-stress curves for martensite and carburized austenite

factor has to be considered because of the limitations of nanoindentation measurement. In addition to the non-ideality of the indent tip and the different assumptions previously discussed, both the pairing of the indents, which relies on the assumption that the material under each indent is perfectly identical, and the heterogeneities of the microstructure increase the scatter of the data. The reliability of this method is nonetheless better in the martensitic band, where the grain size ( $<10 \mu\text{m}$ ) is smaller than the indent tip size, compared to the carburized austenite. Because of the coarse microstructure in the austenitic side (grain size up to  $100 \mu\text{m}$ ), with nanoindentation, only one grain can be probed at the same time and the orientation effects cannot be neglected. The important hardening in the second subregion and the anisotropic behavior of the material also increase the difficulty of extracting plastic properties from nanoindentation tests since the induced stress state and plastic zone around the indent are 3 dimensional [34, 35].

### Comparison with Tensile Tests on Crossweld Specimens and *In-situ* Tensile Tests

The parametric study on the yield stress of the hard layer (martensite and carburized austenite) performed with a numerical model of the crossweld specimen gave an average value for both martensitic and carburized austenite layers of 1800 MPa. This value is in good agreement with the values measured by nanoindentation [1] in the martensitic

band (1650 MPa) and the first subregion of the carburized austenite (2300 MPa), which is a first validation of these results.

However, it must be reminded that the determined value of 1800 MPa represents an indication of the yield behavior of the hard layer, without taking into consideration the possible heterogeneities within the layer and the distinction between the martensitic layer and austenitic zone mechanical behaviors, which are significantly different, as nanoindentation and *in-situ* tensile tests results showed. Moreover, the hard layer can only be characterized by this method for a very limited strain range ( $<3\%$ ). This is due to the smooth tensile specimen failure in the austenitic buttering before any large strain could be measured in the hard layer which was a direct consequence of the presence of two much softer layers (decarburized HAZ and austenitic buttering) around the interface.

On the other hand, *in-situ* tensile tests performed on micro-specimens machined in the hard layer at a submicron scale allowed to characterize the martensitic and carburized austenitic layers for larger strain ranges. The values obtained for  $\sigma_y$  and  $n$  with the *in-situ* tensile test conducted on a martensitic specimen are in a good agreement with the other characterization methods. For the carburized austenite however, a significant difference is observed between nanoindentation measurement [1] and the conducted *in-situ* tensile test (Fig. 18). It must be noted nonetheless that the values extracted from the developed tensile device offer only a qualitative indication of the plastic behavior of the martensitic layer and the carburized austenite. The size-dependance of crystal plasticity has not been investigated in this study and the effect of the grains number and orientation should be consequent at this scale. For the martensitic layer, the grain size ( $<10 \mu\text{m}$ ) is small compared to the specimen size, so the test should be representative of the macroscopic behavior. For the carburized austenite however, the specimen contained a single austenitic crystal, making the plastic behavior dependent on the crystal orientation and size. With that being said, the same tensile test could be numerically simulated with other austenitic

**Table 2** Mechanical properties from nanoindentation by Bucaille's method [1]

	E (GPa)	$\sigma_y$ (MPa)	n
Martensite	244	1472-1797	0
Carburized austenite (15 $\mu\text{m}$ from martensite)	235	2166-2509	0
Carburized austenite (40 $\mu\text{m}$ from martensite)	235	964-1021	0.11-0.13

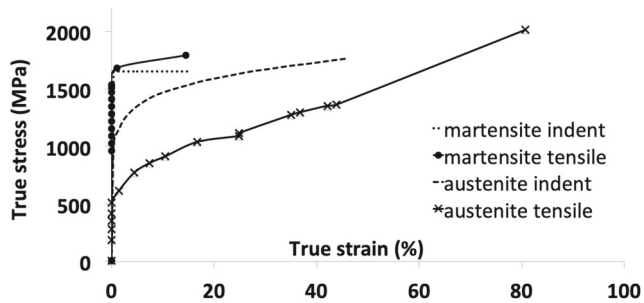


**Fig. 18** Comparison between true strain-stress curves for martensite and carburized austenite from nanoindentation measurement [1] (martensite indent and austenite indent) and *in-situ* tensile tests (martensite tensile and austenite tensile)

crystal orientations using crystal plasticity data on the same material grade. Furthermore, the mechanical behaviors of single crystal specimens and polycrystals were compared by Vo [22] for a 304 stainless steel and a very good agreement was found.

Figure 18 shows a comparison between true stress-strain curves obtained with Berkovich-cube corner nanoindentation measurements [1] and *in-situ* tensile tests. The yield stress calculated from the bimaterial tensile test and associated to carburized austenite (620 MPa) is significantly smaller than the value obtained with nanoindentation (2300 MPa in the first subregion and 1000 MPa in the second subregion). This difference can be explained by several factors. First of all, the advantageous crystal orientation of the austenitic grain in the bimaterial specimen along the tensile axis could lead to an early slip band activation and therefore to a lower yield strength of the material. The anisotropic behavior of the carburized austenitic layer is also another factor which contributes to the deviation of nanoindentation stress-strain state from uniaxial tensile test. Weaver et al. [36] showed in fact that the scaling factor which represents the difference of stress state between spherical nanoindentation and uniaxial tensile test depends on the material anisotropy. Therefore, for an unirradiated 304 stainless steel, a modification of the stress-scaling factor from 2.2 to 2.9 was necessary to obtain a good agreement between spherical nanoindentation and uniaxial tensile test stress-strain curves. As for Berkovich nanohardness, Weaver et al. [36] noted that the conversion of hardness to strength is also inherently dependant on the work hardening behavior of the material because of an important plastic deformation under the sharp indent tip during hardness measurements. Strength values measured with Berkovich nanoindentation were therefore significantly higher than those extracted from uniaxial tensile tests and the authors conclude that Berkovich hardness measurements are limited for uniaxial tensile properties characterization.

In this case, considering the difference in stress state for carburized austenite between nanoindentation and micro-tensile test (Fig. 18) is not sufficient to obtain a good agreement between true stress-strain curves since the measured work hardening exponent of this layer is quite different between both methods (0.25 for the micro-tensile test and 0.12 for nanoindentation). As underlined in the previous work [36], this difference is likely due to the limitations of Berkovich nanohardness, and in the same way of cube corner nanoindentation since the generated plastic deformation is similar, to obtain a representative uniaxial stress-strain response for materials with substantial work hardening.

We can therefore conclude that *in-situ* tensile testing is more suitable than Berkovich-cube corner nanoindentation to characterize the mechanical behavior of the carburized austenitic layer since tensile properties of materials with substantial work hardening are poorly predicted by Berkovich and cube corner nanoindentation. On the other hand, the important work hardening of the carburized austenitic layer during the *in-situ* tensile test allows an accurate measurement of plastic strain up to failure using DIC calculation on the FIB induced marking.

For the martensitic layer, the test results are in a very good agreement with nanoindentation (1680 MPa vs 1650 MPa) (Fig. 18) and also with macroscopic tensile testing (1800 MPa). This agreement is mainly due to a much smaller grain size and to a homogenous behavior in the martensitic band, and also to the small work hardening capacity of this layer, which was correctly predicted by both nanoindentation and *in-situ* tensile testing.

## Conclusion

In this study, an *in-situ* tensile testing device was developed for meso-scale specimens and used to characterize the mechanical behavior of the interface hard layer in a stainless steel dissimilar metal weld. The measured tensile properties for the martensitic band and the carburized austenitic layer from tests on FIB machined micro-samples were compared to nanoindentation measurements [1] and to macroscopic tensile tests on crossweld specimens.

- The laser measurement system of the local diameter evolution (described in [24]) during the loading of the crossweld specimen allows a precise description of true stress and strain values in the hard layer, and combined with a parametric numerical analysis using a finite element model of the specimen, gives a good estimation of the yield stress of the hard layer compared to nanoindentation results. However, the information given by this method in the hardening phase is very

limited because of the small strain range in the hard layer at failure of the specimen.

- FIB machined micro-samples can be used in order to accurately evaluate the tensile properties of "homogeneous" microscopic layers in welds such as the martensitic band in the SS DMW interface. However, the grain size of the tested layer has a significant influence on the results.
- For the martensitic layer which contains small laths compared to the specimen dimensions, the test results are in a very good agreement with nanoindentation and also with macroscopic tensile testing.
- For microscopic layers with important grain size and significant mechanical heterogeneity such as the carburized austenitic layer in SS DMW, the different methods provide different results, which is mainly due to the limitations of nanoindentation measurements for anisotropic layers with coarse microstructure and to grain size dependence of *in-situ* tensile tests.
- DIC measurement with FIB induced marking was found to be an accurate tool to calculate strain distributions in different layers of bimaterial tensile specimens.
- An approximative evaluation of strain and stress to failure and an observation of crack surfaces were possible using the developed *in-situ* tensile testing device.
- Carburized martensite in the SS DMW interface was found to have a very low hardening capacity and important yield stress compared to the ferritic HAZ.
- The carburized austenite in the SS DMW interface keeps a high hardening capacity and ductility even though its yield stress is much higher than that of the austenitic buttering.

We can therefore conclude that *in-situ* tensile testing is a very promising technique for plastic behavior characterization of small scale materials and local hard layers. This technique has also the benefit of characterizing the materials up to failure which allows the analysis of the failure mechanisms.

**Acknowledgments** This work was carried out within the MATMECA consortium and supported by the ANR under contract number ANR-10-EQPX-37.

The presented study was sponsored by Framatome with the participation of the MSSMat and CEA/LISN laboratories. The authors wish to express their gratitude to all the partners who contributed in this work, especially Olivier Ancelet and Gregory Perez (CEA/LISN) for their help and contribution in the experimental program on the DMW mock-up, Éric Perrin and Frédéric Douit (MSSMat) for their great participation in the *in-situ* tensile testing machine development and all the Material research team of MSSMat for their helpful advices.

## Compliance with Ethical Standards

**Conflict of interests** The authors declare that they have no conflict of interest.

## References

1. Mas F (2014) Solidification and phase transformations in a dissimilar steel weld 18MND5/309L/308L : evolution of microstructure and mechanical properties. PhD. Grenoble University
2. Mas F, Martin G, Lhuissier P, Bréchet Y, Tassin C, Roch F, Todeschini P, Simare A (2016) Heterogeneities in local plastic flow behavior in a dissimilar weld between low-alloy steel and stainless steel. *Mater Sci Eng A* 667:156–170
3. Mas F, Tassin C, Valle N, Robaut F, Charlot F, Yescas M, Roch F, Todeschini P, Bréchet Y (2016) Metallurgical characterization of coupled carbon diffusion and precipitation in dissimilar metal welds. *J Mater Sci* 51(10):4864–4879
4. Gilles P, Robin V, Fontaine M (2009) Welding residual stress effect on dissimilar metal weld junction fracture. Conference: ICPVT
5. Blouin A, Chapuliot S, Marie S, Niclaeys C, Bergheau J-M (2014) Brittle fracture analysis of dissimilar metal welds. *Eng Fract Mech* 131:58–73
6. Faidy C (2004) Structural Integrity of dissimilar welds : ADIMEW project overview. In: Proceedings of PVP 2004 asme pressure vessel and piping conference, 2004, USA
7. Gilles PH, Devaux J, Faidy C (2004) ADIMEW Project: Prediction of the ductile tearing of a cracked 16 dissimilar welded junction. In: Proceedings of PVP2004 ASME pressure vessel and piping conference, 2004, USA
8. Klueh RL, King JF (1982) Austenitic stainless steel - ferritic steel weld joint failures. *Weld J* 61:302–311
9. Sun Z, Moisio T (1994) Weld metal/ferritic steel interface in laser welded austenitic/ferritic dissimilar steel joints. *J Mater Sci Lett* 13:802–805
10. Gittos MF, Gooch TG (1992) The interface below stainless steel and nickel-alloy claddings. *Welding Research Supplement*, 461s–472s
11. Duppont JN, Kusko CS (2007) Technical Note: Martensite formation in austenitic/ferritic dissimilar alloy welds. *Welding Journal*, 51s-54s
12. Ornath F, Soudry J, Weiss BZ (1981) Weld pool segregation during the welding of low alloy steels with austenitic electrodes. *Weld J* 60:227–230
13. Ikawa H, Shin S, Inui M, Takeda Y, Nakano A (1972) On the martensitic-like structure at weld bond and the macroscopic segregation in weld metal in the welded dissimilar metals of  $\alpha$ -steels and  $\gamma$ -steels. *IIW Database*, 1–33
14. Kravtsov TG, Ikonnikov VI, Solyanik NK (1989) Structure of the metal in the fusion zone in depositing austenitic steel on pearlitic steel. *Weld Int* 3:200–202
15. Pan C, Wang R, Gui J (1990) Direct TEM observation of microstructures of the austenitic/carbon steels welded joint. *J Mater Sci* 25:3281–3285
16. Gauzzi F, Missori S (1988) Microstructural transformations in austenitic-ferritic transition joints. *J Mater Sci* 23:782–789
17. Murugan N, Parmar RS (1997) Effect of welding conditions on microstructure and properties of type 316L stainless steel





- submerged arc cladding. *Welding Research Supplement*, 210s–217s
18. Swindeman RW, Boiling E (1989) Relaxation response of A533B Steel from 25 to 600°C. Metals and ceramics division, Oak Ridge National Laboratory, Oak Ridge, Tennessee 37831
  19. Kiener D, Grosinger W, Dehm G, Pippan R (2008) A further step towards an understanding of size-dependent crystal plasticity: In-situ tension experiments of miniaturized single-crystal copper samples. *Acta Mater* 56:580–92
  20. Bhattacharyya D, Wheeler RW, Harrison RP, Edwards L (2014) The observation of slip phenomena in single crystal Fe samples during in-situ Micro-Mechanical testing through orientation imaging. *Microsc Microanal* 20:1060–9
  21. Reichardt A, Ionescu M, Davis J, Edwards L, Harrison RP, Hosemann P, Bhattacharyya D (2015) In situ micro tensile testing of He+2 ion irradiated and implanted single crystal nickel film. *Acta Mater* 100:147–154
  22. Vo HT, Reichardt A, Frazer D, Bailey N, Chou P, Hosemann P (2017) In situ micro-tensile testing on proton beam-irradiated stainless steel. *J Nucl Mater* 493:336–342
  23. Katsuhiko F, Fukuya K (2011) Development of micro tensile method in an FIB system for evaluating grain boundary strength. *Mater Trans* 52:20–24
  24. Ancelet O, Matheron P (2010) Development of a new measurement system for tensile testing. PVP2010-25667, Bellevue; 2010
  25. Ben Salem G (2019) Brittle fracture of stainless steel dissimilar metal welds in the brittle-to-ductile transition range. PhD. Paris Saclay University
  26. Giannuzzi LA, Michael JR (2012) Ion channelling vs. electron channelling image contrast. *Microsc Microanal* 18:694–695
  27. Prasath Babu R, Irukuvarghula S, Harte A, Preuss M (2016) Nature of gallium focused ion beam induced phase transformation in 316L austenitic stainless steel. *Acta Mater* 120:391–402
  28. Basa A, Thaulow C, Barnoush A (2013) Chemically induced phase transformation in austenite by focused ion beam. *Metall Mater Trans A* 45(3):1189–1198
  29. Knipling KE, Rowenhorst DJ, Fonda RW, Spanos G (2010) Effects of focused ion beam milling on austenite stability in ferrous alloys. *Mater Charact* 61(1):1–6
  30. Bourcier M, Bornert M, Dimanov A, Héripré E, Raphanel JL (2013) Multiscale experimental investigation of crystal plasticity and grain boundary sliding in synthetic halite using digital image correlation. *J Geophys Res Sol Earth* 118(2):511–526
  31. Allais L, Bornert M, Bretheau T, Caldemaison D (1994) Experimental characterization of the local strain field in a heterogeneous elastoplastic material. *Acta metall mater* 42(11):3865–3880
  32. [www.cast3m.cea.fr](http://www.cast3m.cea.fr)
  33. Bucaille JL, Stauss S, Felder E, Michler J (2003) Determination of plastic properties of metals by instrumented indentation using different sharp indenters. *Acta Mater* 51:1663–1676
  34. Hosemann P, Kiener D, Wang Y, Maloy SA (2012) Issues to consider using nanoindentation on shallow ion beam irradiated materials. *J Nucl Mater* 425:136–9
  35. Kasada R, Takayama Y, Yabuuchi K, Kimura A (2011) A new approach to evaluate irradiation hardening of ion-irradiated ferritic alloys by nano-indentation techniques. *Fusion Eng Des* 86:2658–61
  36. Weaver JS, Pathak S, Reichardt A, Vo HT, Maloy SA, Hosemann P, Mara NA (2017) Spherical nanoindentation of proton irradiated 304 stainless steel: a comparison of small scale mechanical test techniques for measuring irradiation hardening. *J Nucl Mater* 493:368–379

**Publisher's Note** Springer Nature remains neutral with regard to jurisdictional claims in published maps and institutional affiliations.

